In: 2023 AIAA Aviation and Aeronautics Forum and Exposition (AIAA AVIATION Forum), 12-16 June 2023, San Diego, CA.
DOI: 10.2514/6.2023-3394

Experimental Investigation of External Fan Cowl Separation for Compact Nacelles in Windmilling Scenarios

Kshitij Sabnis* and Holger Babinsky†
Department of Engineering, University of Cambridge, Cambridge, CB2 1PZ, UK

Luca Boscagli‡ and David MacManus§
Centre for Propulsion Engineering, Cranfield University, Cranfield, MK43 0AL, UK

Christopher Sheaf¶
Installation Aerodynamics, Rolls–Royce plc, Derby, DE24 8BJ, UK

The slim fan cowl profiles used for ultra-high bypass ratio aircraft engines are designed considering off-design operating conditions, such as engine windmilling during take-off climb out or during cruise. The current paper describes wind tunnel experiments studying how incoming Mach number and engine mass-flow rate influence the aerodynamics governing external fan cowl flow separation in both these windmilling scenarios. A transonic region may form on the forebody surface if the engine becomes inoperative during take-off climb out, with peak Mach number up to 1.2. The subsequent adverse pressure gradient can separate the local boundary layer, resulting in flow separation which originates near the highlight and a more uniform fan cowl pressure distribution. Meanwhile, engine shut down during cruise results in a large supersonic region on the external fan cowl surface which terminates in a normal shock wave. When the Mach number of this shock exceeds about 1.35, a closed separation bubble develops, which causes up to a four-fold increase in the boundary-layer thickness downstream of the shock wave.

I. Introduction

The nacelle design process for civil aircraft requires that both the external fan cowl and internal intake are designed considering off-design operating conditions. The nacelle geometry is typically optimised for the cruise phase of flight, when the stagnation point is located on the internal lip of the nacelle, just inside the highlight, such that there is no boundary-layer separation (Fig. 1a) [1, 2]. However, during high-incidence climb at take-off, the significant angle of incidence causes the stagnation point on the lower aeroline to move outboard, as depicted in Fig. 1b. The substantial surface curvature around the lip can cause the flow inside the intake to become supersonic. This locally supersonic region terminates in a normal shock which can separate the internal boundary layer, causing a stagnation pressure loss and increasing the distortion of flow entering the engine (Fig. 1b) [3]. However, other off-design scenarios can feature flow separation around the external nacelle surface, such as when the engine operates under windmilling conditions [4]. This might occur during the take-off climb out phase of flight, when the aircraft is at a relatively low Mach number but a high angle of attack (Fig. 1c), or during cruise when the aircraft is operated at a higher Mach number but much lower incidence angle (Fig. 1d). The nominal Mach number and incidence angles for the windmilling scenarios in Fig. 1 are based on ETOPS certification for long-range aircraft – end-of-runway windmilling occurs at 20 degree nacelle incidence and Mach 0.25 [4] whilst diversion windmilling corresponds to 4.5 degree nacelle incidence and incoming Mach 0.65 [5].

In both these scenarios, the mass flow through the engine reduces and therefore the stagnation point moves inside the nacelle lip. In the climb out case, termed 'end-of-runway windmilling', Fig. 1c shows that as the stagnation point is shifted internally, the imposed streamline curvature around the high-curvature lip causes additional flow acceleration.

*Research Associate, Department of Engineering, University of Cambridge.
†Professor of Aerodynamics, Department of Engineering, University of Cambridge, AIAA Fellow.
‡Research Fellow, Centre for Propulsion Engineering, Cranfield University.
§Professor of Propulsion Aerodynamics, Centre for Propulsion Engineering, Cranfield University.
¶Installation Aerodynamics Specialist, Installation Aerodynamics, Rolls–Royce plc.

a) cruise
(4.5° incidence, Mach 0.85)

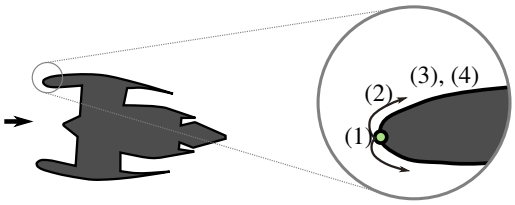

(1) stagnation point around lip highlight
(2) local flow acceleration is moderate
(3) no shock waves or strong adverse pressure gradient
(4) no internal or external boundary layer separation

b) high-incidence climb
(23° incidence, Mach 0.45)

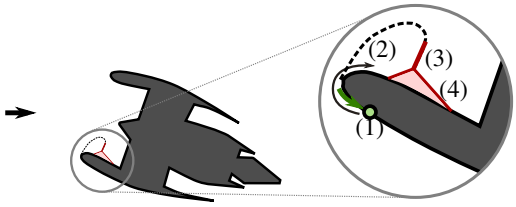

(1) stagnation point at bottom aeroline moves outboard
(2) curvature causes flow acceleration to supersonic
(3) supersonic region terminates in normal shock
(4) shock pressure rise separates boundary layer

c) end-of-runway windmilling
(20° incidence, Mach 0.25) [4]

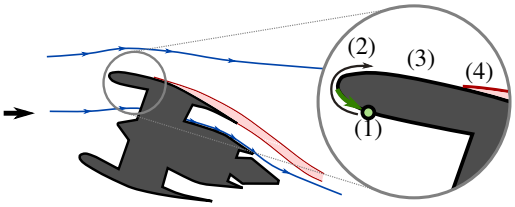

(1) stagnation point at top aeroline moves inboard
(2) curvature causes flow acceleration to severe suction peak
(3) boundary layer experiences adverse pressure gradient
(4) external cowl boundary layer separates

d) diversion windmilling
(4.5° incidence, Mach 0.65) [5]

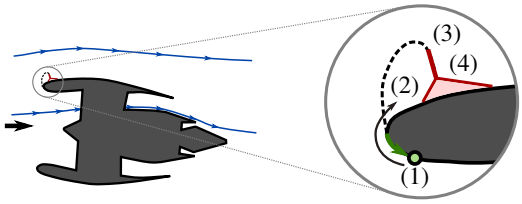

(1) stagnation point at top aeroline moves inboard
(2) curvature causes flow acceleration to supersonic
(3) supersonic region terminates in normal shock
(4) shock pressure rise separates boundary layer

Fig. 1 Schematic of flow separation mechanisms for different on-design and off-design conditions.

As a result there is a substantial suction peak, and the boundary layer is then exposed to a more severe adverse pressure gradient to meet the trailing-edge pressure condition. This can cause flow separation on the external upper surface of the nacelle. On the other hand, Fig. 1d describes the situation, termed 'diversion windmilling', when an engine is shut down during the cruise phase of flight. The higher Mach number in this scenario means that the flow tends to locally become supersonic when it accelerates around the nacelle lip. The terminating normal shock then imposes a strong adverse pressure gradient which can separate the boundary layer on the external nacelle surface.

Whether caused by subsonic diffusion or a normal shock, any significant detachment of the boundary layer around the upper external fan cowl surface during engine windmilling needs to be assessed. In a situation where thrust has been lost due to engine-out, this separation increases the drag and could result in adverse interactions with the wing flow field [4], which is especially relevant for configurations where the engine is installed close to the wing. The conventional approach has been to stay away from regimes with detrimental flow separation by designing conservative fan-cowl profiles with only moderate curvature around the highlight. However, the need to improve propulsive efficiency and reduce emissions under the constraints of current technology requires the use of ultra-high bypass ratio (UHBR) engine technology. These engines use significantly larger fans, which require the engine nacelles to also be increased in cross-section. However, in order to prevent a corresponding increase in drag due to a larger wetted area, these UHBR nacelles need to be more compact by minimising both thickness and length while satisfying aerodynamic design requirements [6, 7]. As a result, the nacelle lip geometries necessarily feature higher local curvature and are therefore more prone to separation in off-design conditions [1, 8]. It is therefore important to be able to understand the aerodynamics underlying the flow separation behaviour around compact nacelle geometries.

The flow physics describing internal nacelle separation in the high-incidence climb phase of flight (Fig. 1b) has been studied extensively using both experiment and computation [3, 9, 10], and so is relatively well understood. However, there has been comparatively little research into nacelle aerodynamics in windmilling scenarios (Figs. 1c and 1d), with no fundamental experimental investigation of this flow field in the literature. The problem is further compounded by the computational RANS methods typically used in industry being unable to reliably predict these complex flows [10, 11]. In order to address this gap of knowledge and improve aerodynamic understanding of this flow field, a series of wind tunnel experiments are performed using a quasi-two-dimensional setup which replicates windmilling conditions for a representative UHBR nacelle geometry.

II. Research Methodology

A. Experimental facility

The experimental rig to investigate external fan cowl separation is integrated into a blow-down transonic wind tunnel at the University of Cambridge. The wind-tunnel assembly, which is schematically depicted in Fig. 2 is fed from a high-pressure reservoir into the settling chamber, where it passes through a number of flow straighteners and turbulence grids, followed by an 18:1 contraction with a round-to-rectangular transition. The test section, which is 114 mm wide and 1200 mm long, consists of an underlying tunnel structure, marked in light gray in Fig. 2, onto which custom-built liner blocks (dark gray) are bolted. The sidewalls of the wind tunnel are formed by removable doors containing two optical-access windows with 203 mm diameter, which are indicated in Fig. 2. The stagnation pressure can be set up to a maximum of 200 kPa, which permits some control over the Reynolds number of the flow in the test section.

The wind-tunnel model is based on a representative 3D non-axisymmetric baseline nacelle, which is designed for a long-range aircraft at $M_\infty = 0.85$ with a compact, dual separate jet exhaust [8]. The nacelle itself is left–right symmetric and four degrees of freedom are applied to each of five control aerolines at 45-degree intervals from top to bottom. Appropriate values for these key nacelle dimensions are determined with a fully parametric definition that uses the intuitive class-shape transformation (iCST) method [12, 13]. The design process is based on a multi-point, multi-objective optimisation routine based on a well-established CFD methodology [8]. Each nacelle is assessed using 3D computations of the full-scale geometry at six operating conditions, including the design cruise condition and both windmilling scenarios [5]. The initial Latin hypercube sampling (LHS) design space exploration uses 400 candidate geometries. The subsequent optimisation procedures evaluate 7450 different nacelle geometries, from which a Pareto front is constructed. The nacelle designs are then down-selected to a single geometry which minimises cruise drag whilst requiring that the length of any separation is less than 5% of the nacelle length, L_{nac} [8].

Two different rigs are used to study diversion windmilling and end-of-runway windmilling, as shown in Figs. 2b and 2c, respectively. Both rigs use the same nacelle model which is defined by the top aeroline of the three-dimensional nacelle geometry. A chordwise coordinate, s, is defined in Figs. 2b and 2c to be in the outward direction from the highlight along the external fan cowl surface. This coordinate is typically normalised by the chordwise nacelle length, L_{nac}, which is 415 mm for the diversion rig and 423 mm for the end-of-runway rig.

The contours of the tunnel liner blocks in Fig. 2 are based on a vertical planar slice through 3D RANS simulations of the representative nacelle geometry for the diversion windmilling and end-of-runway windmilling conditions, respectively. The ceiling and floor liner contours are defined by streamlines extracted from this plane above and below the nacelle, respectively. This process is illustrated schematically in Fig. 3 for both the windmilling scenarios under consideration, with the design process explained in detail in Ref. [14]. Note that the geometry has been inverted from the physical engine, such that the upper wall contour is representative of a streamline that is captured within the engine whereas the lower wall is based on a streamline external to the nacelle. As a result, the external fan cowl surface of interest constitutes the lower surface of the nacelle model. Such an arrangement improves the interface with the existing tunnel structure and reduces the curvature of the liner contours, thereby reducing the likelihood of problems associated with tunnel wall separation or unwanted supersonic regions.

To account for the differences in area variation between the two-dimensional tunnel and the three-dimensional engine, the lower bounding streamline is adjusted to match the target pressure distribution on the nacelle's external surface. An initial Latin Hypercube Sampling (LHS) with 25 samples is conducted, with the lower bounding streamline described parametrically using iCST [12] to finely control the lower channel area distribution. This process is performed using the three-dimensional test rig computations which incorporate the tunnel sidewalls and therefore account for the effects of the tunnel wall boundary layers [14].

There is an airfoil located downstream of the test section, as labelled in Fig. 2a. The flow at this point is choked to

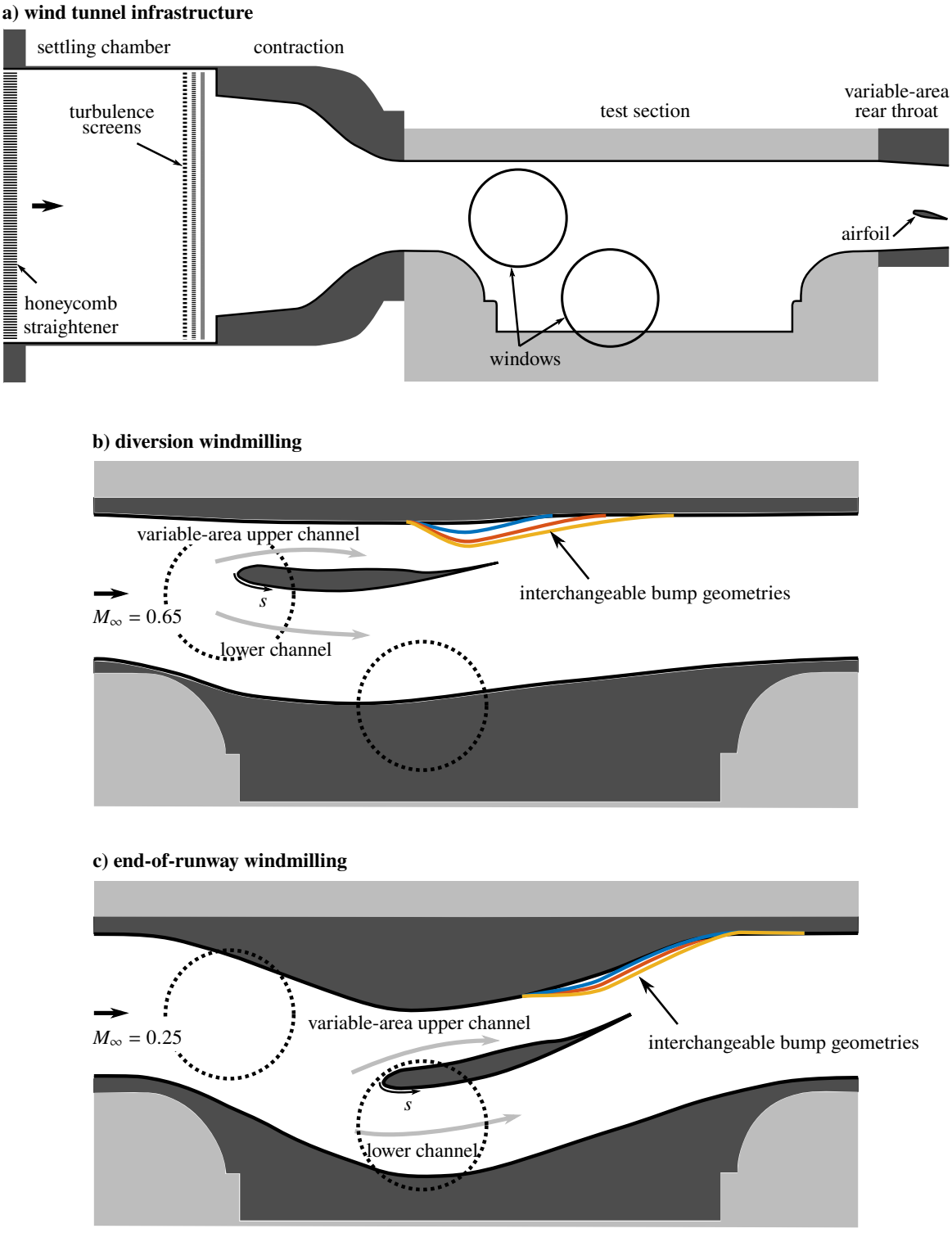

Fig. 2 Schematic of the wind tunnel facility into which the nacelle rig is integrated and detail of test sections for both windmilling rigs.

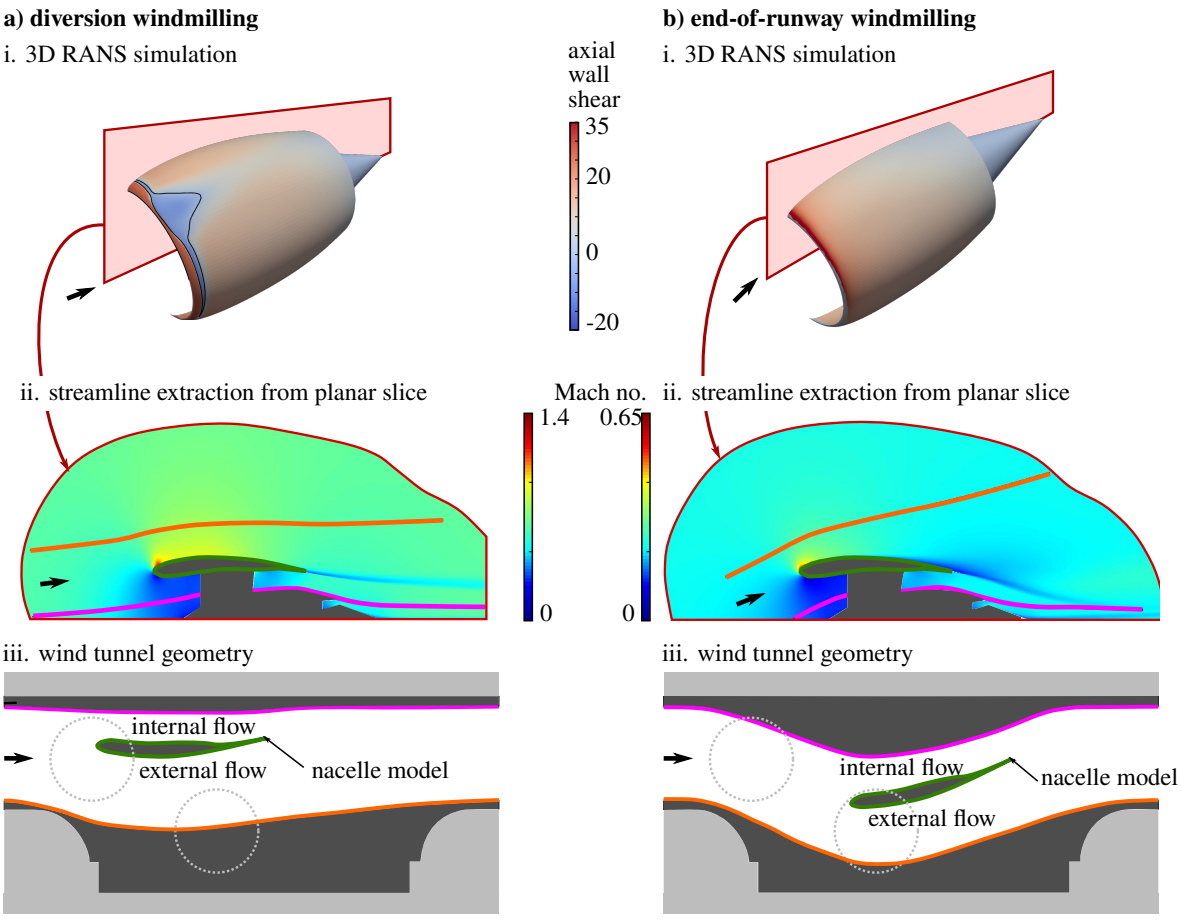

Fig. 3 Schematic generation of the rig geometry for both windmilling scenarios, with tunnel wall contours defined by streamlines extracted from a planar slice of 3D computations.

form a 'rear throat'. The area ratio between this rear throat and the test-section inlet determines the entry Mach number. Thus, by varying the angle of the airfoil, the inlet Mach number is controlled. In the test section itself (Figs. 2b and 2c), the nacelle model splits the test section flow into two channels. By changing the relative mass flows through each channel, it is possible to replicate variations in the mass flow demand of the engine under windmilling conditions. This mass flow split is controlled by installing interchangeable 'bumps' with different heights onto the upper wall. These bumps which throttle the flow in this channel and thus prescribe the upper-channel mass flow rate. Note that the upper channel is not choked, but instead the mass flow split is controlled by making the subsonic flow respond to imposed changes in the channel area.

There are three mass flow cases considered for the diversion windmilling scenario, which are parameterised by the ratio between the height of the bump from a nominal streamline internal to the engine (h_b) and the vertical height of the tunnel in the entry plane (Δy). The bumps installed for the diversion windmilling rig have $h_b/\Delta y = 0.159$, 0.194 and 0.227, which correspond to decreasing effective engine mass flow rates and are thus termed 'mild', 'moderate' and 'strong' windmilling, respectively. Similarly, the end-of-runway windmilling rig is studied at three separate engine mass flow conditions, with $h_b/\Delta y = 0.286$, 0.311 and 0.340 chosen to correspond to 'mild', 'moderate' and 'strong' windmilling.

For the diversion windmilling scenario, structural constraints dictate that a 1/14th nacelle model is the largest scale which can feasibly be installed into the test section. Nevertheless, the fact that the facility is pressurised means that the Reynolds number based on nacelle lip thickness, 1.2×10^6, is only a factor of three lower than the full-scale value. However, whilst transitional RANS computations indicate that the full-scale nacelle exhibits a turbulent boundary layer

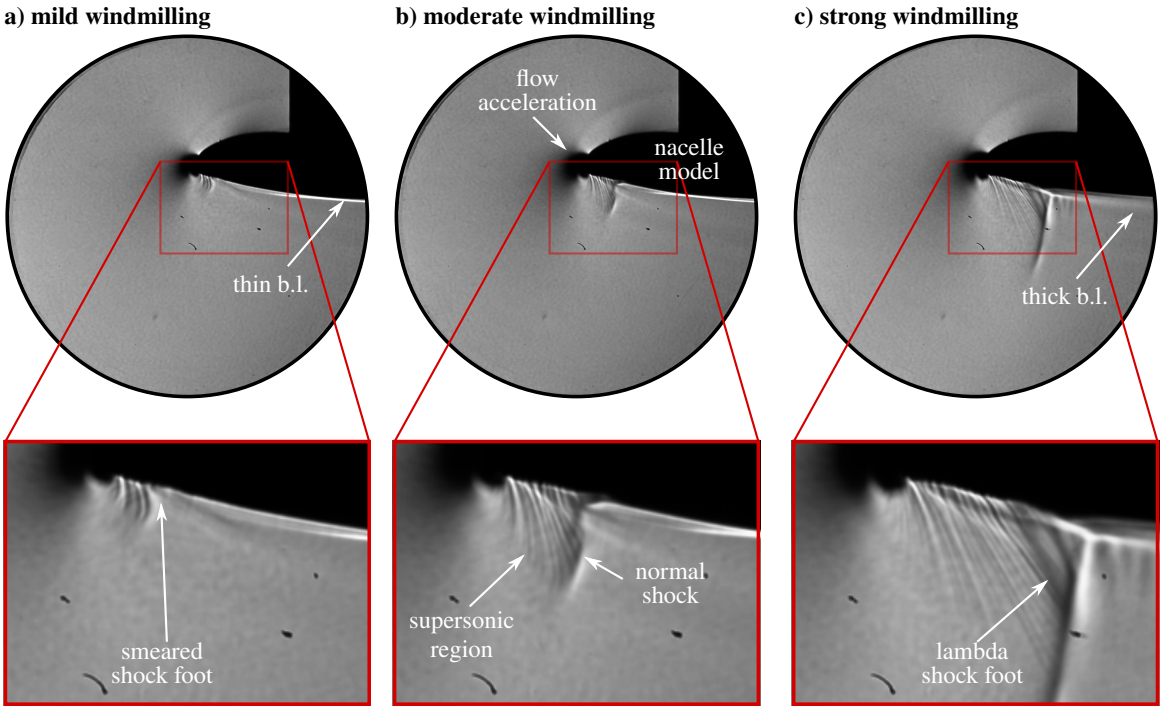

Fig. 4 Schlieren visualisation of diversion windmilling flow field at Mach 0.65.

ahead of the shock wave, a laminar interaction is observed at the reduced rig Reynolds number [15]. In agreement with this prediction, infrared thermography of the external fan cowl surface on a prototype nacelle model reveals a temperature distribution characteristic of a laminar shock–boundary-layer interaction (SBLI). Therefore, in order to replicate the turbulent interaction expected for the full-scale nacelle, the wind tunnel model is modified by locally increasing the surface roughness in a small region around the leading edge from 2 microns to 30 microns in order to promote transition. Infrared thermography data has shown this approach to be successful in producing a turbulent SBLI on the external fan cowl surface [15]. Note that, for the end-of-runway windmilling scenario, the 1/12th scale model which is used matches the Reynolds number ($\mathrm{Re}_t = 1.65 \times 10^6$) for a full-scale nacelle in the relevant phase of flight.

B. Measurement techniques

A z-type schlieren system with a horizontal knife-edge enables visualisation of spanwise-averaged density gradients associated with flow features, such as boundary layers and shock waves. For each configuration, schlieren images are captured at 6400 frames per second using a Photron Fastcam Nova S6 camera, with an exposure time of 12.5 µs. The flow fields presented in the current paper are a time average of 1800 consecutive frames.

Steady-state surface pressure distributions are measured using pressure-sensitive paint (PSP). The surface of interest is sprayed with a special polymer binder seeded with luminescent molecules. When irradiated by UV light, the resultant luminescence intensity ratio ($I_{\mathrm{ref}}/I(p,T)$) is dependent on the local pressure, as specified by the Stern–Volmer relation [16]:

$$\frac{I_{\mathrm{ref}}}{I(p,T)} = A(T) + B(T)\frac{p}{p_{\mathrm{ref}}} \tag{1}$$

The luminescence is recorded using a RaspberryPi camera module 3 which has a Sony IMX708 sensor. The reference condition is taken with the wind tunnel off, such that $p_{\mathrm{ref}} = 101$ kPa everywhere. In order to determine the values of $A(T)$ and $B(T)$ in the Stern–Volmer relation, in-situ calibration is performed using at least ten 0.3 mm diameter static pressure taps connected to a differential pressure transducer (error: ±1%) [17]. This calibration enables absolute pressure values on the target surface to be extracted from the measured light intensity. A comparison between static tap pressures and the calibrated PSP data places an error bound of 5% on these measurements. However, in regions

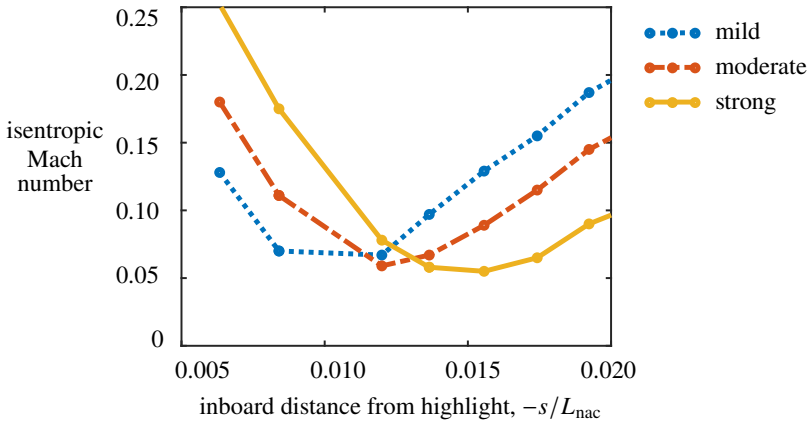

Fig. 5 Isentropic Mach number around the stagnation point for diversion windmilling at Mach 0.65.

where the thermal properties change (e.g. filler material or attachment screws) or where reflections from the tunnel walls distort the measured luminescence, the calibration is no longer valid and a much greater error is observed.

The topology of the separated flow field is surveyed using the time-averaged skin-friction lines from surface oil-flow visualisation. This technique involves coating the surface of interest with a mixture made from paraffin, finely-powdered titanium dioxide, oleic acid and lubricating oil. There is a small error due to oil-flow producing an inaccurate indication of separation location, by about 0.2 local boundary-layer thicknesses = 0.6 mm [18]. Furthermore, preliminary measurements indicate that the intrusive oil layer changes the nature of the end-of-runway windmilling flow field, and thus the technique is not suitable for this rig. Nevertheless, oil-flow visualisation do allow the flow topology in the diversion windmilling rig to be determined, and comparisons of the size of separation regions between different setups are considered to be reliable.

Point measurements of local flow velocity are provided by two-component laser Doppler velocimetry (LDV). The flow is seeded with paraffin in the settling chamber; previous measurements of particle lag through a normal shock have placed the seeding droplet diameter in the range 200 − 500 nm [17]. The error in measured velocities due to the finite number density of seeding particles and due to the laser optics is 2% for away from the wall, increasing to approximately 20% in the immediate vicinity of the nacelle model surface. In practice, LDV is not precisely a point-measurement technique, since velocities are averaged over a nominal ellipsoidal probe volume which spans 0.1 mm in the streamwise and vertical directions, and 2 mm in the spanwise direction. The positional accuracy of this probe volume is, approximately, $\Delta x \approx 0.2$ mm, $\Delta y \approx 0.005$ mm, and $\Delta z \approx 0.1$ mm.

Boundary-layer traverses are carried out with wall-normal resolution roughly 0.1 mm. The measured boundary-layer data is fitted to theoretical profiles. A Sun & Childs (1973) fit [19], adapted to include a van Driest compressibility correction, is used for the outer layer; this combines a log-law of the wall region with a Coles wake function. The viscous sublayer is modelled using a Musker (1979) fit [20]. These fitted profiles are then used to calculate characteristic boundary-layer integral parameters. This avoids errors caused by poor measurement resolution near the wall and therefore provides a more accurate estimate of integral boundary-layer parameters. The boundary-layer properties are determined in their incompressible forms, as these are less sensitive to variations in Mach number and require fewer assumptions to calculate from raw velocity data. The LDV data obtained in this study typically has around 40 measurement points within the boundary layer and the closest data point to the wall is at around $y^+ = 80$. This corresponds to an uncertainty in integral parameters of around 5% for an equilibrium turbulent boundary layer [21].

III. Diversion Windmilling

A. Nominal conditions: Mach 0.65

Figure 4 presents schlieren visualisation of the diversion windmilling flow field for all three effective engine mass-flow rates. The dark region immediately upstream of the lip highlight is related to the optical distortion caused by the substantial density gradients in this region. Further downstream, the supersonic region can be visualised by the presence

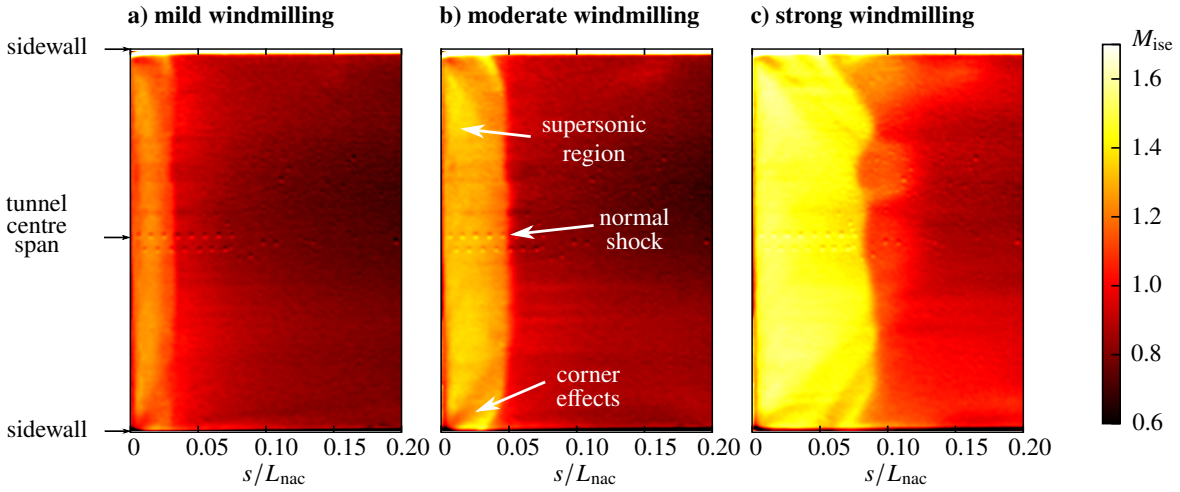

Fig. 6 Mach number distribution from PSP on the external surface for diversion windmilling at Mach 0.65.

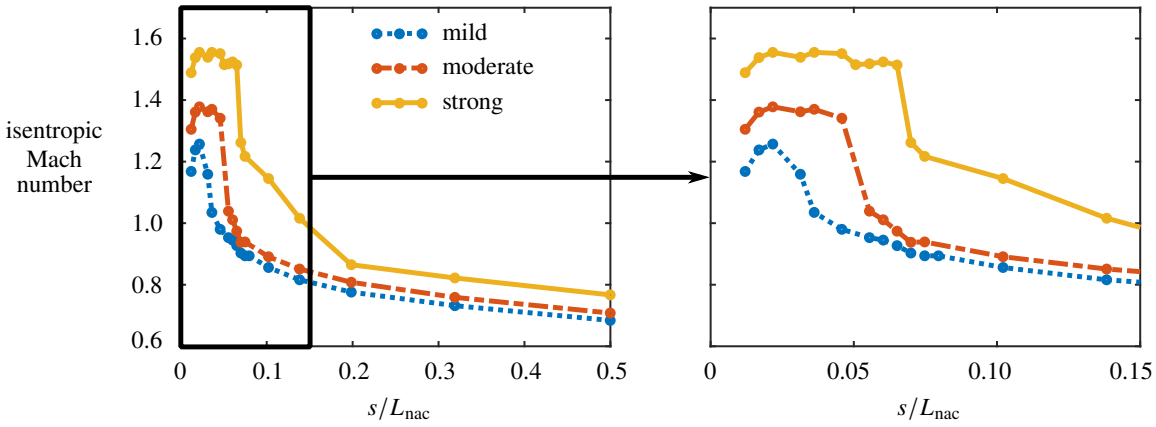

Fig. 7 Mach number on the centre span of the external surface for diversion windmilling at Mach 0.65.

of weak waves emanating from the lower model surface, which corresponds to the external fan cowl. This supersonic region is terminated by a normal shock, which appears in the schlieren images as a dark line approximately normal to the external fan cowl surface. The boundary layer downstream of the shock can be identified as a bright region which develops along the external nacelle surface.

As the windmilling severity is increased, representative of decreased mass flow through the engine, Fig. 4 shows that the supersonic region grows in size as the normal shock moves downstream. In addition, the structure of the shock–boundary-layer interaction progresses from a characteristic attached interaction with a smeared shock foot in Fig. 4a to a lambda-shock structure typical of a separated SBLI (Fig. 4c). A close examination of sequential frames of the instantaneous flow field for the intermediate case (moderate windmilling) suggests that the boundary layer is incipiently separated. An explanation for the observed changes in flow field as the effective engine mass-flow rate is reduced can be derived from a series of static pressure taps located roughly on the tunnel centre span around the stagnation point on the internal nacelle surface (Fig. 5). The stagnation point corresponds to the location where the isentropic Mach number reaches a minimum. As the windmilling severity is increased, Fig. 5 reveals that the stagnation point moves by about 0.005 L_{nac} further inside the internal surface of the nacelle. This movement can be attributed to the larger bump height throttling the flow within the upper channel and so the dividing streamline is closer to the tunnel's upper wall, equivalent to a reduced engine mass-flow rate.

The effect of the increased windmilling strength on the flow over nacelle's external surface is demonstrated by the

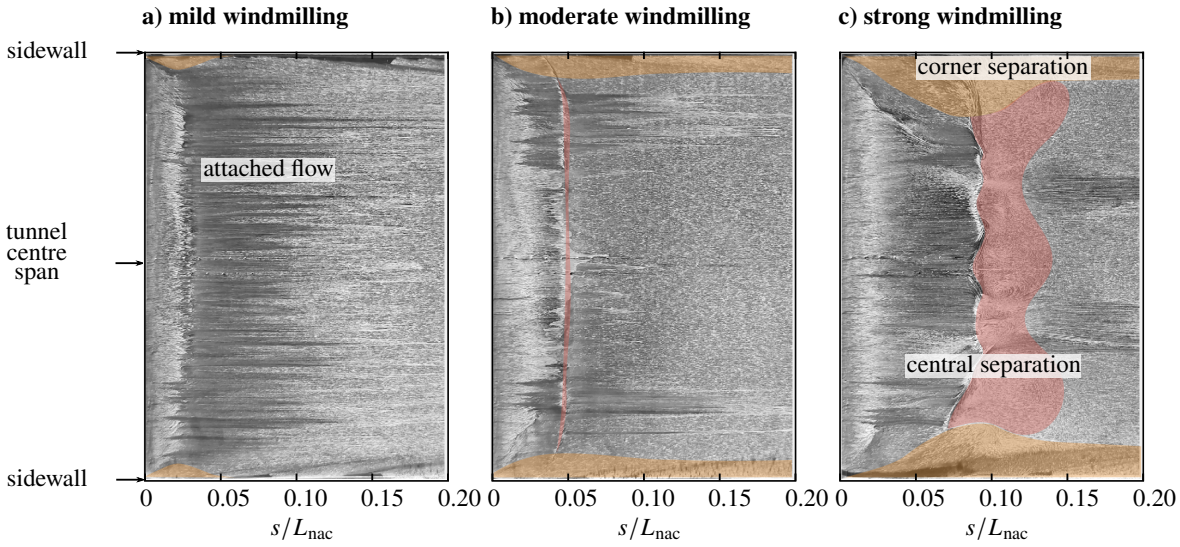

Fig. 8 Surface oil-flow visualisation on the external surface for diversion windmilling at Mach 0.65.

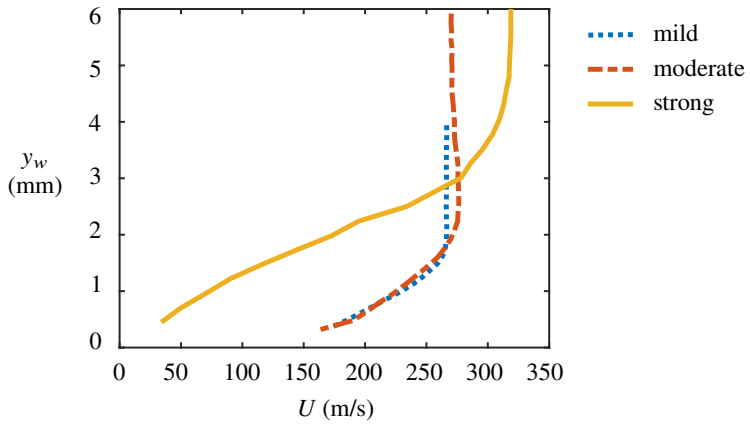

Fig. 9 Boundary-layer profiles from LDV at $s = 0.14L_{\mathrm{nac}}$ for diversion windmilling at Mach 0.65.

Table 1 Integral parameters for boundary-layer profiles in Fig. 9 (diversion windmilling at Mach 0.65).

windmilling severity	boundary-layer thickness, δ (mm)	displacement thickness, δ_i^* (mm)	momentum thickness, θ_i (mm)	shape factor H_i
mild	1.81	0.36	0.24	1.51
moderate	2.12	0.40	0.27	1.48
strong	4.69	1.59	0.75	2.11

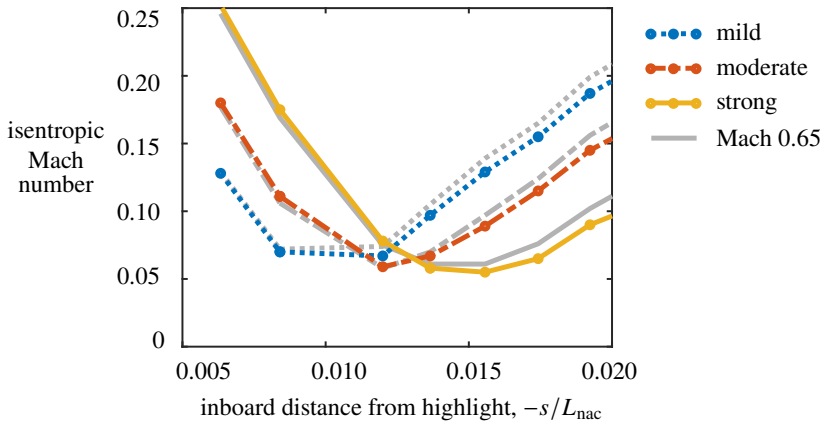

Fig. 10 Isentropic Mach number around the stagnation point for diversion windmilling at Mach 0.60.

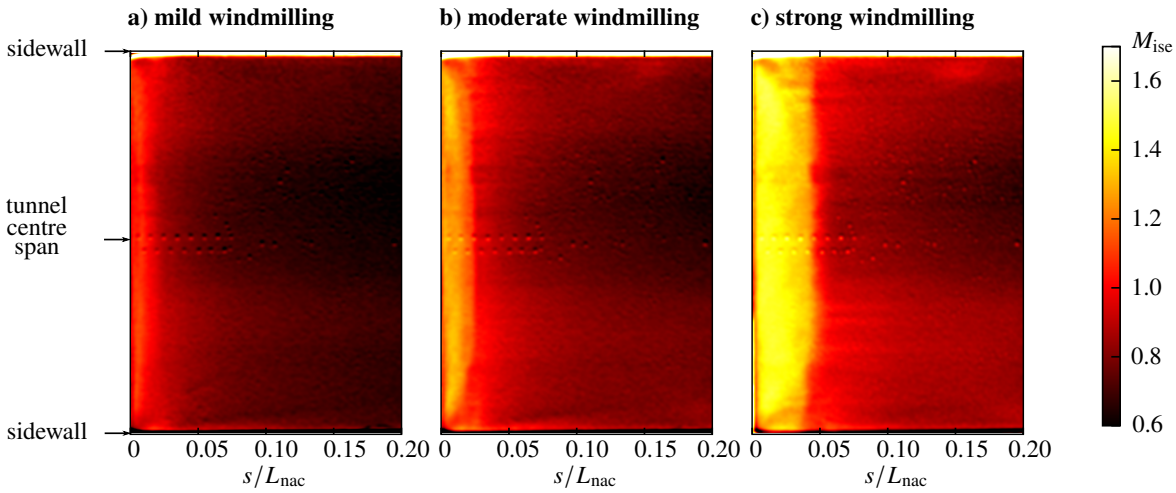

Fig. 11 Mach number distribution from PSP on the external surface for diversion windmilling at Mach 0.60.

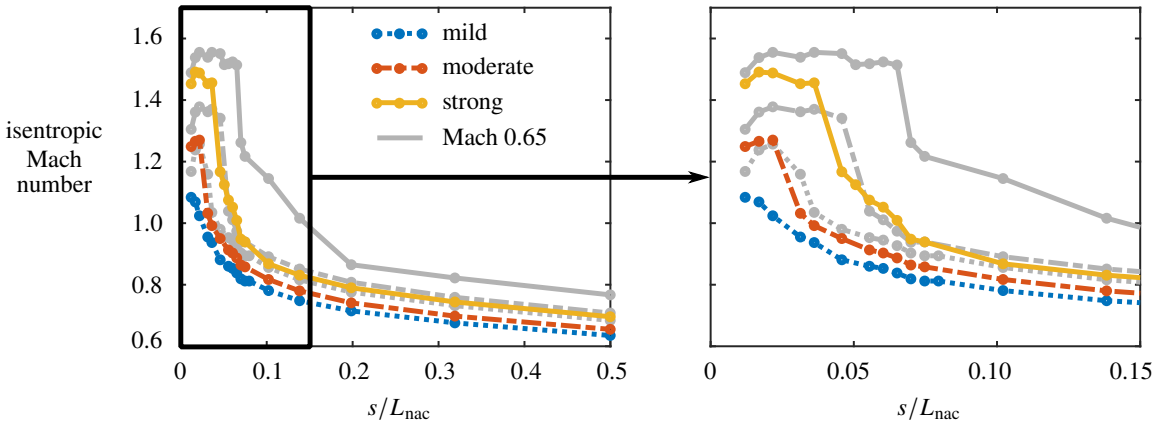

Fig. 12 Mach number on the centre span of the external surface for diversion windmilling at Mach 0.60.

Table 2 Integral parameters for boundary-layer profiles in Fig. 14 (diversion windmilling at Mach 0.60).

windmilling severity	boundary-layer thickness, δ (mm)	displacement thickness, δ_i^* (mm)	momentum thickness, θ_i (mm)	shape factor H_i
mild	1.77	0.33	0.23	1.48
moderate	1.97	0.37	0.25	1.47
strong	3.35	0.59	0.41	1.44

surface pressure distribution depicted in Fig. 6. All three cases show a supersonic region terminating in a normal shock which is roughly uniform across the span of the tunnel. As the windmilling severity increases and the stagnation point moves inboard on the nacelle, Fig. 6 shows that the supersonic region becomes larger in size. In addition the Mach number immediately upstream of the shock increases, corresponding to a stronger normal shock wave. This behavioural trend can be quantified using static tap data along the tunnel centre span. Figure 7 shows that, from mild to moderate windmilling, the shock moves downstream by approximately $0.02L_{\text{nac}}$ and its strength increases from $M_s = 1.25$ to 1.36. A further change to strong windmilling causes the shock to move downstream by a further $0.02L_{\text{nac}}$ and to become even stronger, with $M_s = 1.55$. The reason for the increase in shock strength is related to the flow being accelerated by a larger portion of the highly-curved contour as the stagnation point moves inwards. As a result, there is a higher Mach number in the supersonic region, which produces a stronger normal shock. In order for this normal shock to meet the trailing edge pressure condition, it is necessary for its position to move further downstream.

The subsequent effects of the increase in shock Mach number are evident in the oil-flow visualisation presented in Fig. 8. The position of the shock wave is evident in 8a from an accumulation of oil corresponding to a sudden reduction in shear stress. Nevertheless the streamlines everywhere (except for a small region near the corners) are in the streamwise direction, indicating that the boundary layer remains attached for this case. For moderate windmilling, Fig. 8b reveals separation across much of the span of the tunnel which extends less than 0.005 L_{nac} in the chordwise direction. In addition, noticeable corner separation has begun to develop near the tunnel sidewalls. Finally, the strong windmilling case exhibits more substantial separation in Fig. 8c. The streamwise separation length on the tunnel centreline has increased to 4.5% of the nacelle length and has become more three dimensional, while the corner separation has also become larger.

The differences in separation behaviour for the three cases are reflected in the boundary-layer state downstream of the SBLI, which is measured using LDV. Figure 9 shows that, at $s/L_{\text{nac}} = 0.14$, the boundary-layer profiles for the three cases appear to be quite different. The mild windmilling case, where the boundary layer remained attached through its interaction with the shock wave, exhibits a very thin boundary layer. As listed in Table 1, the incompressible displacement thickness, δ_i^*, for this case only 0.36 mm. The incipiently-separated case has a slightly thicker boundary layer at this station, with $\delta_i^* = 0.40$ mm. Finally the strong windmilling case with substantial shock-induced separation exhibits a boundary layer almost four times as thick ($\delta_i^* = 1.59$ mm). Note that these observations can partially be explained by the fact that the boundary layer recovers most quickly immediately downstream of the shock wave, and so its state is a strong function of distance from the interaction (which is different for the three cases). Nevertheless, it is evident that differences in boundary-layer properties caused by the presence of flow separation do persist downstream of any shock wave which exists on the external fan cowl surface.

B. Reduced incoming Mach number: Mach 0.60

In order to assess how the incoming Mach number affects the flow field and underlying physical mechanisms, the equivalent measurements are also collected when the incoming Mach number is reduced from 0.65 to 0.60. Fig. 10 shows that the position of the stagnation point remains essentially unchanged. However, for all three cases, the supersonic region is substantially smaller than for $M_\infty = 0.65$ (Fig. 11. As shown in Fig. 12 the shock wave is also substantially weaker than in the Mach 0.65 case. Indeed, the mild windmilling flow field has such a weak shock that it resembles a series of weak compression waves. These observations are consistent with the schlieren images in Fig. 13, which show a smaller supersonic region than Fig. 4. There is no visible shock wave for the mild windmilling case in Fig. 13a and the shock foot for the strong windmilling scenario (Fig. 13c) is much more smeared, suggesting that the flow field is now attached or incipiently separated.

A reduced entry Mach number causes weaker shock waves because, for a given stagnation point, the same streamline

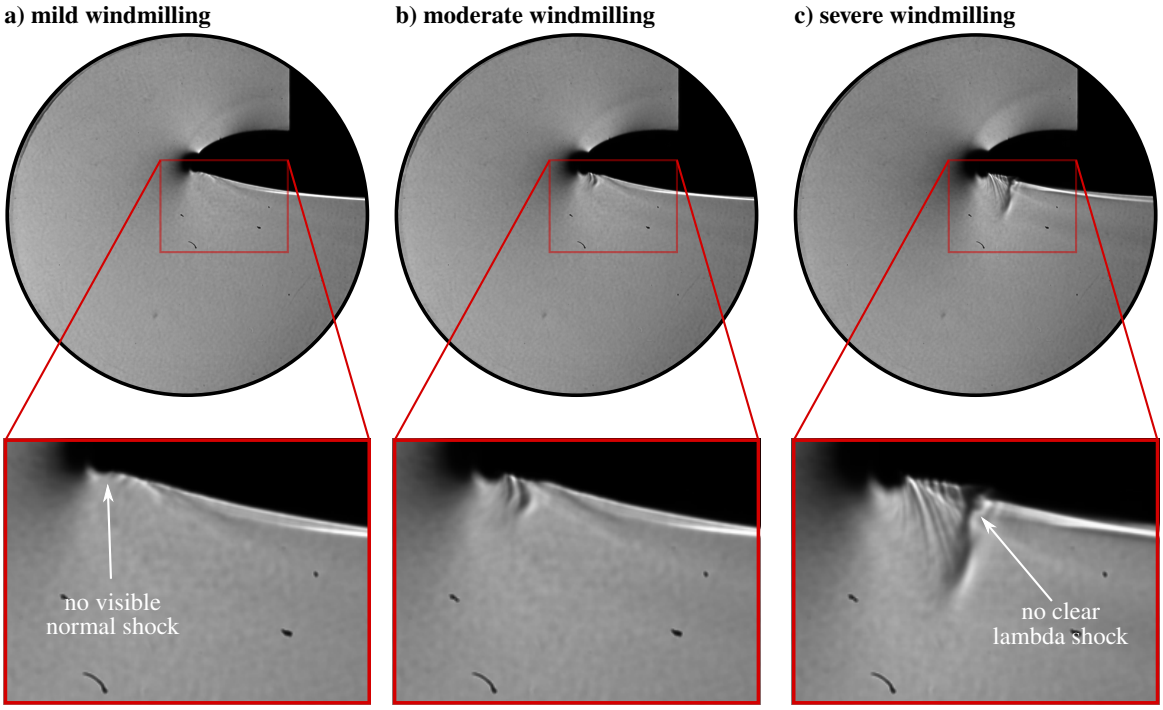

Fig. 13 Schlieren visualisation of diversion windmilling flow field at Mach 0.60.

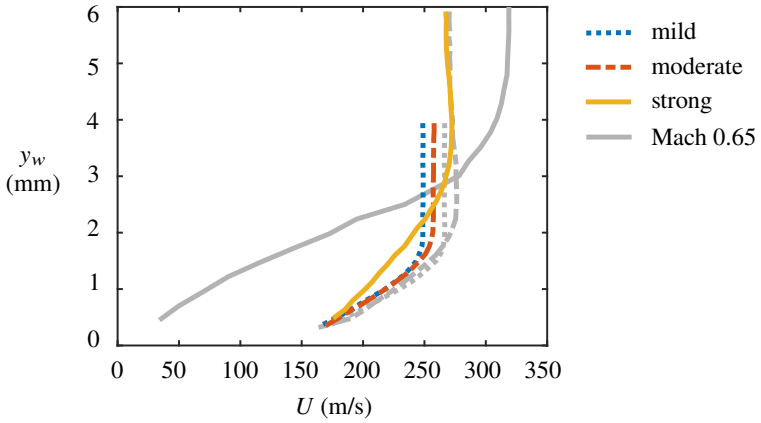

Fig. 14 Boundary-layer profiles from LDV at $s = 0.14L_{\text{nac}}$ for diversion windmilling at Mach 0.60.

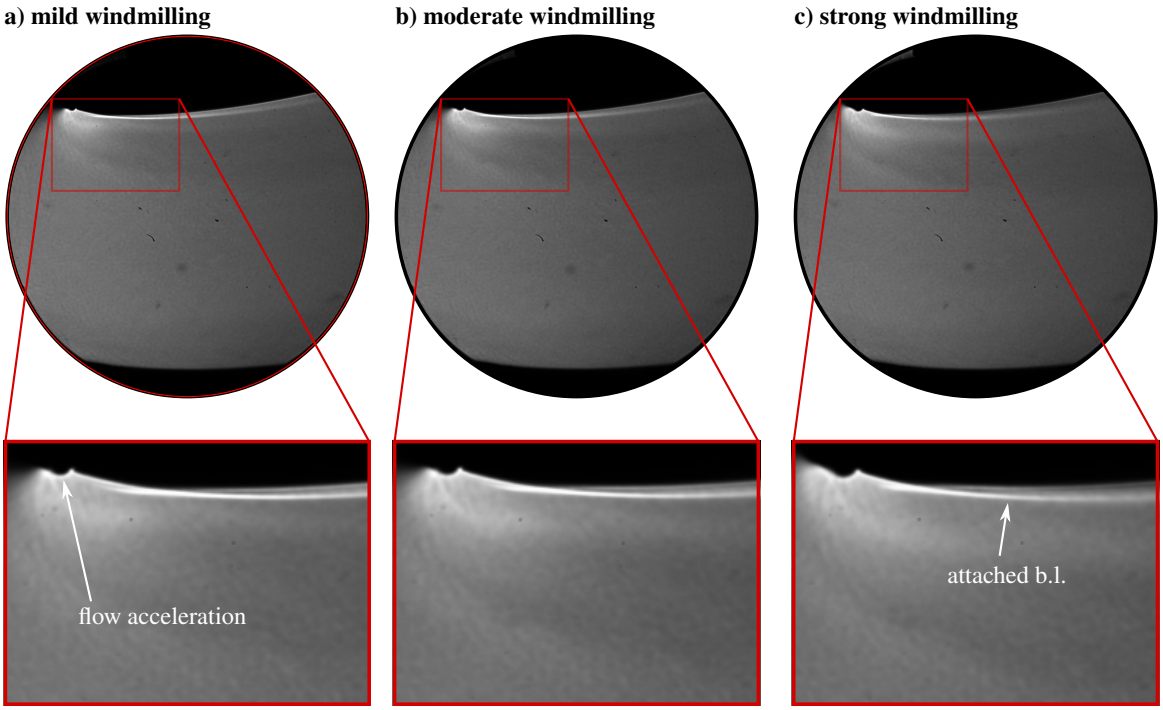

Fig. 15 Schlieren visualisation of end-of-runway windmilling flow field at Mach 0.25.

curvature around the highlight produces roughly the same flow acceleration. Therefore, a lower entry Mach number corresponds to a reduced Mach number supersonic region and thus a weaker shock wave. Despite the weaker shock wave, there is almost no difference in the downstream boundary-layer profile for the mild windmilling case in Fig. 14. This is likely because, for this mass-flow split, both the Mach 0.60 and Mach 0.65 cases correspond to the boundary-layer having always remained attached through the normal shock interaction. The boundary layer for the intermediate case presents a small reduction in boundary-layer thickness compared to the Mach 0.65 case but is otherwise similar in profile. The most pronounced change, however, is for strong windmilling, where the boundary layer is about 60% thinner than at Mach 0.65 and has a much fuller profile (Table 2. The reason for this is that the boundary layer now remains attached through the interaction with the weaker shock, and thus the downstream boundary layer is thinner and has more momentum.

IV. End-of-Runway Windmilling

A. Nominal conditions: Mach 0.25

Figure 15 presents schlieren visualisation of the end-of-runway windmilling flow field. The dark region around the leading edge is caused by optical distortion due to the substantial flow acceleration in this region. The boundary layer developing along the external fan cowl surface can be visualised as a bright area of the flow field. Despite some very subtle differences to the flow field between the three cases – the strong-acceleration region gets bigger and the downstream boundary layer becomes slightly more diffuse with increasing windmilling severity – the flow fields look very similar, with the boundary layer remaining attached.

The position of the stagnation point is shown in Fig. 16 to be at roughly $-s/L_{\text{nac}} = 0.025$. This location is further downstream than for the diversion windmilling scenario, due to the increased nacelle incidence angle under end-of-runway conditions. Progressing from mild to strong windmilling, the stagnation point moves further inside the nacelle lip by $0.008L_{\text{nac}}$ due to the increased restriction of mass flow through the upper channel as the bump height is increased. Similar to the diversion windmilling flow field, there is also a corresponding influence on the external fan cowl surface pressure distribution, as visualised using PSP in Fig. 17. This surface pressure distribution is roughly

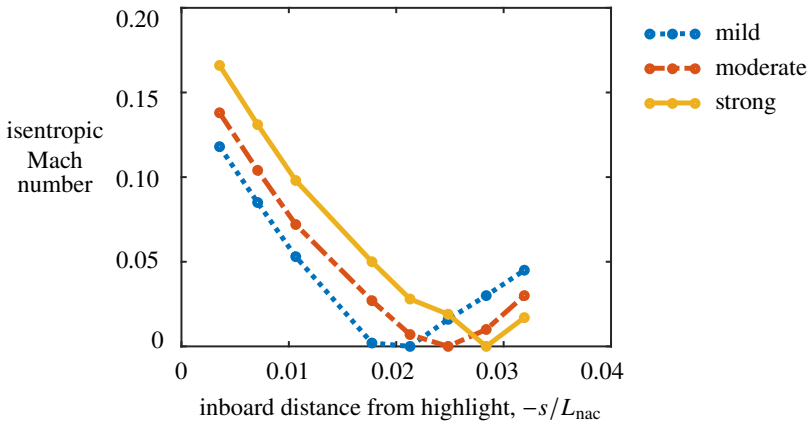

Fig. 16 Isentropic Mach number around the stagnation point for end-of-runway windmilling at Mach 0.25.

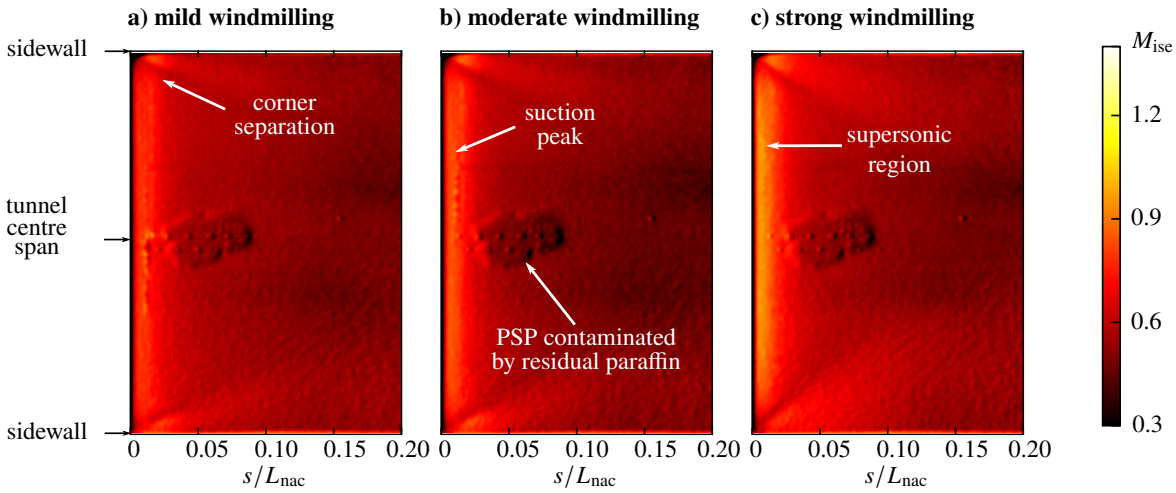

Fig. 17 Mach number distribution on the external surface for end-of-runway windmilling at Mach 0.25.

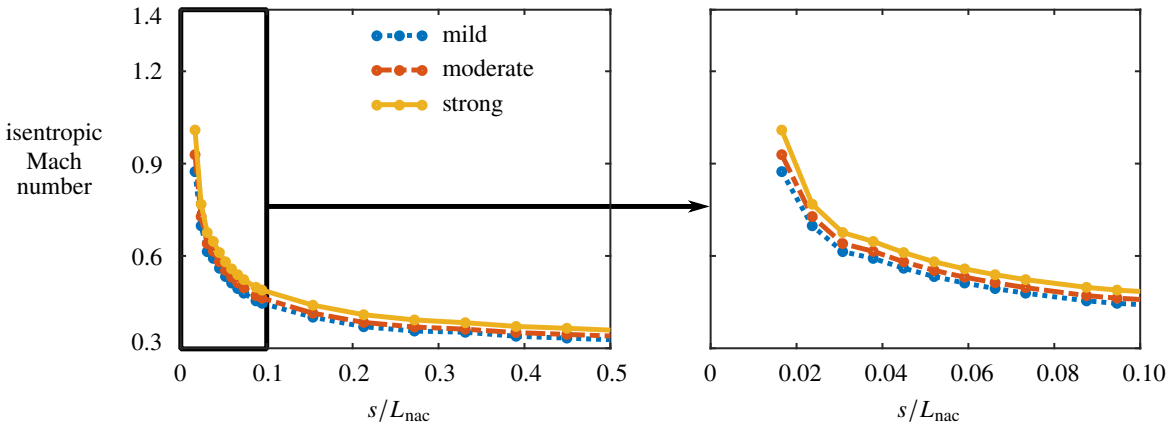

Fig. 18 Mach number on the centre span of the external surface for end-of-runway windmilling at Mach 0.25.

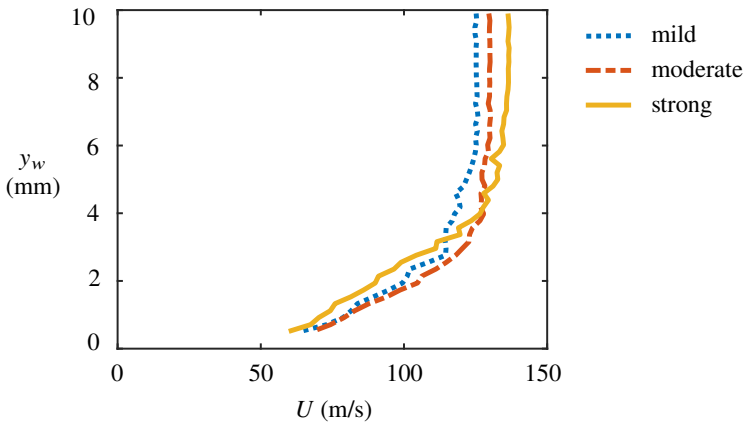

Fig. 19 Boundary-layer profiles from LDV at $s = 0.24L_{\text{nac}}$ for end-of-runway windmilling at Mach 0.25.

Table 3 Integral parameters for boundary-layer profiles in Fig. 19 (end-of-runway windmilling at Mach 0.25).

windmilling severity	boundary-layer thickness, δ (mm)	displacement thickness, δ_i^* (mm)	momentum thickness, θ_i (mm)	shape factor H_i
mild	4.47	0.95	0.62	1.54
moderate	3.97	0.91	0.57	1.60
strong	5.37	1.38	0.82	1.70

two-dimensional across much of the tunnel span, although there is evidence of some corner separation near the sidewalls at the leading edge. As the windmilling severity increases, the suction peak near the leading edge becomes more severe, featuring a higher Mach number at this location.

This trend is reflected in the static pressure tap data along this external fan cowl surface in Fig. 23. The isentropic Mach number values are larger for increased windmilling severity over the entire measured region, consistent with the shifted stagnation point causing greater acceleration around the nacelle leading edge. Although there are no pressure taps close enough to the leading edge to fully resolve the suction peak, the Mach number at the first pressure tap provides an indication of the key behaviour. Similar to the behaviour further downstream, the isentropic Mach number at this location becomes larger with increasing windmilling severity. The Mach number in this region is lower than for the diversion case due to the significantly reduced incoming Mach number. Nevertheless, Fig. 18 demonstrates that a supersonic region can indeed form under end-of-runway conditions, with a measured peak Mach number of 1.05 for the strong windmilling case. Nevertheless, no obvious shock waves can be detected in the schlieren images (Fig. 15) suggesting that there are a series of weak compression waves rather than a normal shock.

Figure 19 presents boundary-layer profiles measured using LDV at $s/L_{\text{nac}} = 0.24$. As the windmilling severity is increased, the freestream velocity becomes larger, which is consistent with the isentropic Mach number distribution in Fig. 18. However, Fig. 19 also shows that the boundary layer becomes considerably thicker as the windmilling severity is increased. For example, the incompressible displacement thickness becomes 45% larger from mild to strong windmilling and the shape factor increases from 1.54 to 1.70. This behaviour is likely caused by the boundary layer thickening in response to the enhanced adverse pressure gradient caused by the strong suction peak and thus containing less momentum.

B. Increased incoming Mach number: Mach 0.30

Structural constraints prevent larger bumps, corresponding to even more severe windmilling, from being installed on the upper wall to investigate the onset of separation at Mach 0.25. Instead, data is collected at a higher incoming Mach number, $M_\infty = 0.30$. Figure 20 presents schlieren images of the flow field. For the mild and moderate windmilling

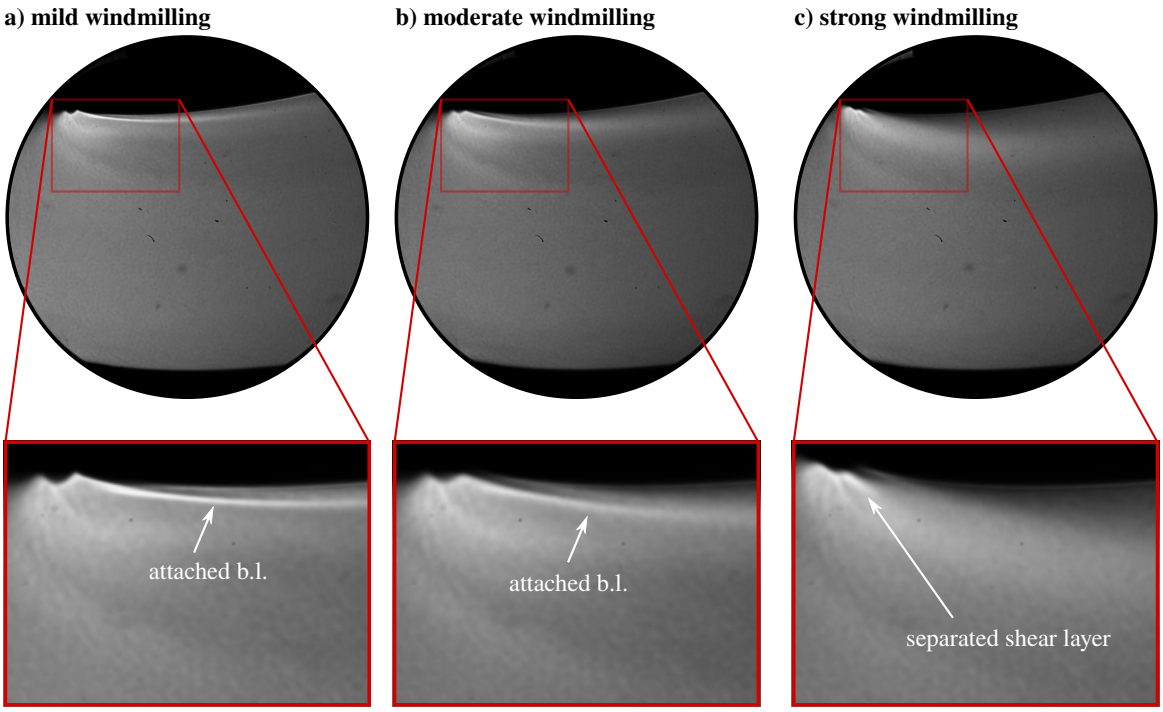

Fig. 20 Schlieren visualisation of end-of-runway windmilling flow field at Mach 0.30.

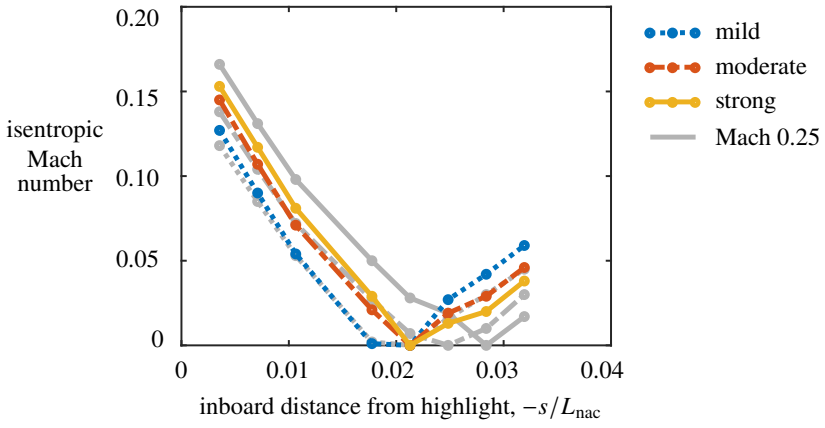

Fig. 21 Isentropic Mach number around the stagnation point for end-of-runway windmilling at Mach 0.30.

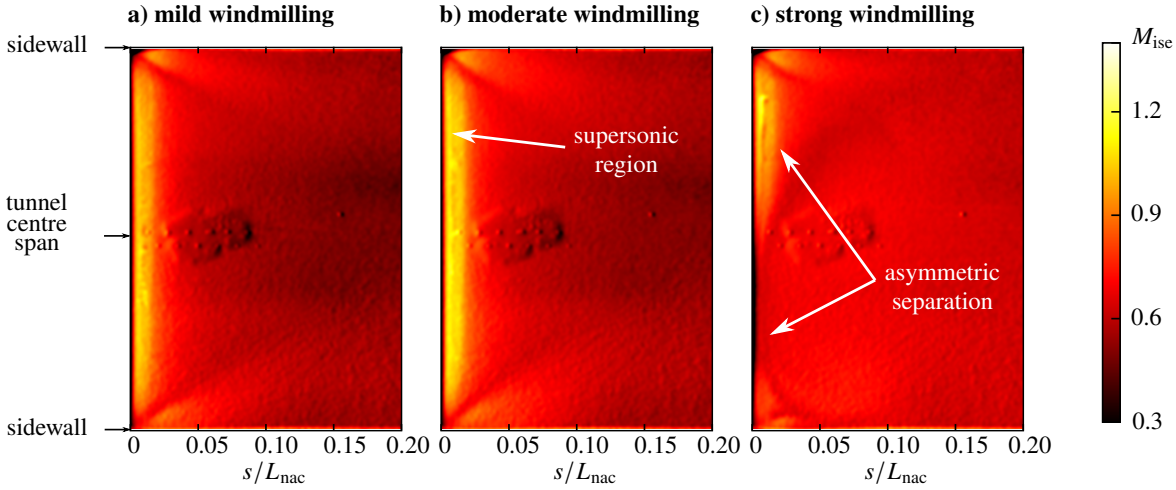

Fig. 22 Mach number distribution on the external surface for end-of-runway windmilling at Mach 0.30.

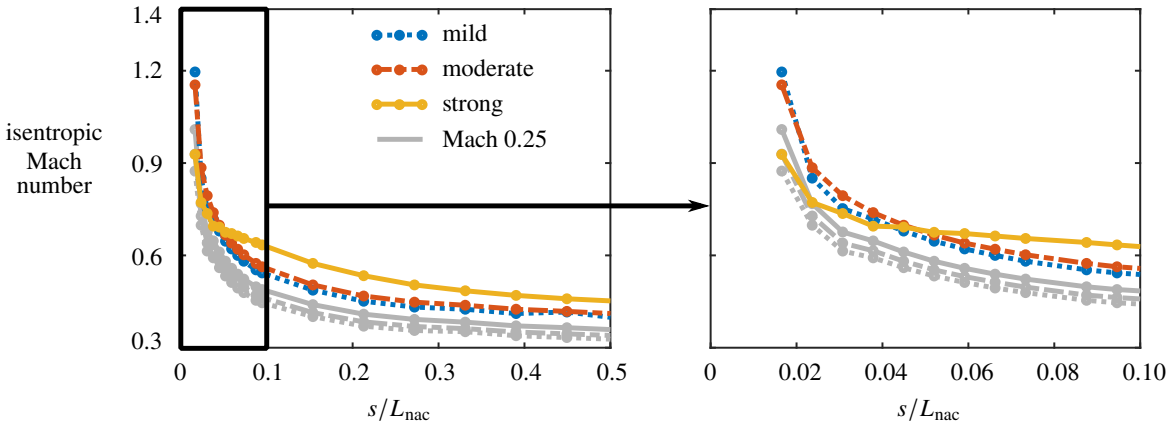

Fig. 23 Mach number on the centre span of the external surface for end-of-runway windmilling at Mach 0.30.

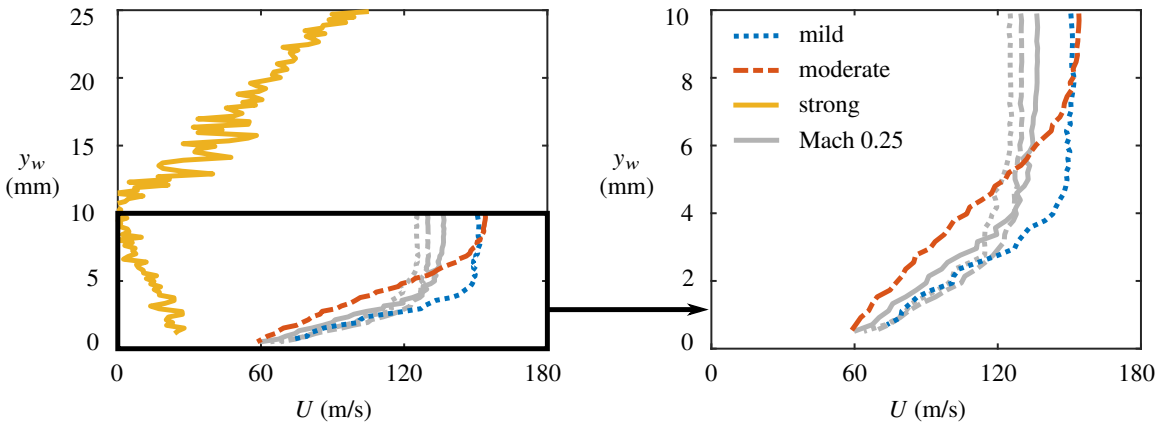

Fig. 24 Boundary-layer profiles from LDV at $s = 0.24L_{\text{nac}}$ for end-of-runway windmilling at Mach 0.30.

Table 4 Integral parameters for boundary-layer profiles in Fig. 24 (end-of-runway windmilling at Mach 0.30). Reliable parameters were not obtained for the strong windmilling case due to the non-equilibrium velocity profile.

windmilling severity	boundary-layer thickness, δ (mm)	displacement thickness, δ_i^* (mm)	momentum thickness, θ_i (mm)	shape factor H_i
mild	5.10	1.37	0.79	1.75
moderate	8.52	2.49	1.35	1.84
strong	–	–	–	–

cases, this figure appears to be broadly similar to the Mach 0.25 flow field (Fig. 20), albeit with a slightly thicker boundary layer. However, the strong windmilling case does look very different, with a separated shear layer originating at the leading edge and no subsequent reattachment.

The position of stagnation point for mild and moderate windmilling is shown in Fig. 21 to correspond well to the equivalent locations at Mach 0.25. However, the position for the strong windmilling case is quite different, being shifted upstream by $0.008s/L_{\text{nac}}$. The pressure distribution on the external nacelle surface in Fig. 22 features a prominent supersonic region for mild and moderate windmilling, with a local isentropic Mach number of roughly 1.2 (Fig. 23). The strong windmilling case, which features significant flow separation appears to be asymmetric across the tunnel span in Fig. 22. The peak Mach number is reduced and the pressure distribution downstream of this location is much more uniform than the attached cases, due to the decambering effect of the separated shear layer.

The boundary-layer profiles at $s/L_{\text{nac}} = 0.24$, presented in Fig. 24. The freestream velocities higher than for $M_\infty = 0.25$ due to the higher incoming Mach number. However, the boundary layer profiles, even for mild and moderate windmilling, are significantly thicker than the equivalent velocity distributions at Mach 0.25. For example, Table 4 lists incompressible displacement thickness values which are as much as 2.7 times thicker than in Table 3. This behaviour is a direct consequence of boundary-layer thickening in response to the enhanced adverse pressure gradient in these flow fields. The boundary layer may also have been subjected to a weak shock wave terminating the supersonic region (albeit not visible in schlieren imaging) which would further increase its thickness. Nevertheless, the most profound change is in the strong windmilling case. Here, the edge of the shear layer cannot be detected using LDV in Fig. 24, even within 25 mm of the nacelle model surface. Furthermore, there is a clear region of reversed flow within the 10 mm region closest to the surface (the LDV data is presented as velocity vector magnitude, so this appears as a positive deviation away from zero velocity in this near-wall region). The vastly different velocity distribution demonstrates the substantial negative effect that flow detachment can have on the boundary-layer development along the external fan cowl surface.

V. Conclusions

This paper presents an experimental study using a novel two-dimensional wind tunnel rig to investigate separation on the external surface of fan cowls for ultra-high bypass ratio engines in two off-design scenarios. End-of-runway windmilling conditions, experienced during take-off climb out, feature low Mach numbers ($M = 0.25$) and high effective angles of attack ($\alpha = 20°$) [4], causing external fan cowl separation through subsonic diffusion. Meanwhile, the higher Mach number ($M = 0.65$) and lower angle of attack ($\alpha = 4.5°$) in windmilling diversion [5], for engine out at cruise, exhibits a supersonic region around the lip and normal shock-induced separation. Understanding separation mechanisms in these scenarios is particularly relevant to UHBR nacelles, which tend to feature more aggressive curvature compared to traditional engine fan cowl geometries. In both scenarios, the likely drag penalty when separation occurs motivates the need to better understand its onset and underlying physical mechanisms. A particular focus of the fundamental wind tunnel study is to investigate the aerodynamic behaviour as the effective engine mass-flow rate and incoming Mach number are varied for each windmilling scenario.

Under nominal diversion windmilling conditions at Mach 0.65, the stagnation point tends to be located on the internal lip of the nacelle. As the engine mass flow rate is reduced, this stagnation point moves further inside the nacelle by roughly 0.5% of the nacelle length for the cases considered in this study. The size of the supersonic region also increases and the terminating normal shock wave strengthens from Mach 1.25 to 1.55. The boundary layer on the external fan cowl surface is able to remain attached through the pressure rise for the weakest of these shock waves, but the Mach 1.55 normal shock wave produces to a separated shock–boundary-layer interaction, with a separation length 0.045 L_{nac}. This separation has a profound effect on the boundary layer developing on the external fan cowl surface, which is up to four times thicker than the boundary layer that remained attached through the interaction. However, when the incoming Mach number is reduced to 0.60, despite the stagnation point position remaining unchanged, the Mach number within the supersonic region is lower. As a result, there is a smaller supersonic region with a weaker normal shock, which means that the flow is less likely to separate and thus the boundary-layer displacement thickness downstream of the shock wave is reduced by as much as 60%.

Nominal end-of-runway windmilling conditions at Mach 0.25 feature attached boundary layers for all three windmilling flow levels under consideration. Within this regime, as the engine mass flow rate is reduced, the stagnation point moves further inside the nacelle, and there is greater acceleration around the nacelle lip. The suction peak on the external fan cowl surface becomes more pronounced and can even feature a small supersonic region, limited to about 2% of the nacelle chord. The stronger suction peak imposes a greater adverse pressure gradient on the external fan cowl boundary layer, with a measured increase in displacement thickness of 45% and increase in shape factor of 10% over the cases studied. When the incoming Mach number is increased to 0.30, the stagnation point for attached flow fields remains unchanged but the peak Mach number on the external fan cowl surface becomes as high as 1.2. The associated increase in adverse pressure gradient downstream of this suction peak causes the boundary layer to almost triple in thickness. For the most severe windmilling case studied, this adverse pressure gradient is sufficient to cause leading-edge separation, where the resulting shear layer does not reattach. The edge of this shear layer is more than six equivalent attached boundary-layer thicknesses away from the nacelle surface at roughly one-quarter of the nacelle chord, and a significant near-wall reversed flow region can be detected. The flow separation causes the Mach number distribution on the external fan cowl surface to become almost uniform and a reduced Mach number of 0.9 is measured at the suction peak. The flow separation also influences the trailing edge pressure condition, which provides a likely mechanism for the observed upstream shift of the stagnation point under separated conditions.

The experiments provide insight into the key mechanisms defining the flow around compact aero-engine nacelles under windmilling conditions during take-off climb out and cruise. The data collected will be used alongside high-fidelity computations of the wind tunnel flow path generated by the ODIN consortium to gain further understanding of the underlying flow physics. The measurements also form a valuable reference data set which will be compared against equivalent RANS computations, which are typically used in industry for nacelle design. Such comparisons will enable an assessment into the capabilities and limitations of existing computational methods to reliably predict key flow parameters, such as the onset of separation, in windmilling scenarios, as required to guide the design of UHBPR nacelles.

Acknowledgements

This project has received funding from the Clean Sky 2 Joint Undertaking (JU) under grant agreement number 101007598. The JU receives support from the European Union's Horizon 2020 research and innovation programme and the Clean Sky 2 JU members other than the Union. The authors would like to thank D. Martin, A. Luckett and C. Costello for operating the blow-down wind tunnel.

References

[1] Tejero, F., Robinson, M., MacManus, D., and Sheaf, C., "Multi-objective optimisation of short nacelles for high bypass ratio engines," *Aerospace Science and Technology*, Vol. 91, 2019, pp. 410–421.

[2] Robinson, M., MacManus, D., Christie, R., Sheaf, C., and Grech, N., "Nacelle design for ultra-high bypass ratio engines with CFD based optimisation," *Aerospace Science and Technology*, Vol. 113, 2021, p. 106191.

[3] Coschignano, A., Babinsky, H., Sheaf, C., and Zamboni, G., "Normal-shock/boundary-layer interactions in transonic intakes at high incidence," *AIAA Journal*, Vol. 57, No. 7, 2019, pp. 2867–2880.

[4] Hoelmer, W., Younghans, J., and Raynal, J., "Effect of Reynolds number on upper cowl flow separation," *Journal of Aircraft*, Vol. 24, No. 3, 1987, pp. 161–169.

[5] Deneys Schreiner, B., Tejero, F., MacManus, D., and Sheaf, C., "Robust aerodynamic design of nacelles for future civil aero-engines," *Turbo Expo: Power for Land, Sea, and Air*, Vol. 84058, American Society of Mechanical Engineers, 2020, p. V001T01A015.

[6] Hughes, C., "The promise and challenges of ultra high bypass ratio engine technology and integration," Tech. Rep. HQ-STI-11-012, National Aeronautics and Space Administration, 2011.

[7] Magrini, A., Benini, E., Yao, H.-D., Postma, J., and Sheaf, C., "A review of installation effects of ultra-high bypass ratio engines," *Progress in Aerospace Sciences*, Vol. 119, 2020, p. 100680.

[8] Swarthout, A., MacManus, D., Tejero, F., Matesanz Garcia, J., Boscagli, L., and Sheaf, C., "A comparative assessment of multi-objective optimisation methodologies for aero-engine nacelles," *33rd Congress of the International Council of the Aeronautical Sciences*, 2022.

[9] O'Pray, C., Babinsky, H., and Sheaf, C., "The influence of surface geometry on the fan-plane boundary-layer in transonic intakes at high-incidence," *AIAA Scitech 2022 Forum*, 2022–1806.

[10] Kalsi, H., and Tucker, P., "Numerical modelling of shock wave boundary layer interactions in aero-engine intakes at incidence," *Proceedings of ASME Turbo Expo 2018 Turbomachinery Technical Conference and Exposition*, Vol. 50985, GT2018-75872, American Society of Mechanical Engineers, 2018.

[11] Oriji, U., and Tucker, P., "Modular turbulence modeling applied to an engine intake," *Journal of Turbomachinery*, Vol. 136, No. 5, 2014, p. 051004.

[12] Christie, R., Heidebrecht, A., and MacManus, D., "An automated approach to nacelle parameterization using intuitive class shape transformation curves," *Journal of Engineering for Gas Turbines and Power*, Vol. 139, No. 6, 2017.

[13] Christie, R., Robinson, M., Tejero, F., and MacManus, D., "The use of hybrid intuitive class shape transformation curves in aerodynamic design," *Aerospace Science and Technology*, Vol. 95, 2019, p. 105473.

[14] Sabnis, K., Babinsky, H., Boscagli, L., Swarthout, A., Tejero, F., MacManus, D., and Sheaf, C., "A wind tunnel rig to study the external fan cowl separation experienced by compact nacelles in windmilling scenarios," *AIAA Scitech 2023 Forum*, 2023-1942.

[15] Sabnis, K., Boscagli, L., Babinsky, H., MacManus, D., and Sheaf, C., "Experimental investigation of transonic external fan cowl separation," *57th 3AF International Conference on Applied Aerodynamics*, 2023, Paper AERO2023-16.

[16] Gregory, J., Asai, K., Kameda, M., Liu, T., and Sullivan, J., "A review of pressure-sensitive paint for high-speed and unsteady aerodynamics. Proceedings of the Institution of Mechanical Engineers," *Part G: Journal of Aerospace Engineering*, Vol. 222, No. 2, 2008, pp. 249–290.

[17] Colliss, S., Babinsky, H., Nübler, K., and Lutz, T., "Vortical structures on three-dimensional shock control bumps," *AIAA Journal*, Vol. 54, No. 8, 2016, pp. 2338–2350.

[18] Squire, L., "The motion of a thin oil sheet under the steady boundary layer on a body," *Journal of Fluid Mechanics*, Vol. 11, No. 2, 1961, pp. 161–179.

[19] Sun, C., and Childs, M., "A modified wall wake velocity profile for turbulent compressible boundary layers." *Journal of Aircraft*, Vol. 10, No. 6, 1973, pp. 381–383.

[20] Musker, A., "Explicit expression for the smooth wall velocity distribution in a turbulent boundary layer," *AIAA Journal*, Vol. 17, No. 6, 1979, pp. 655–657.

[21] Titchener, N., Colliss, S., and Babinsky, H., "On the calculation of boundary-layer parameters from discrete data," *Experiments in Fluids*, Vol. 56, No. 8, 2015, p. 159.

2023-06-08

Experimental investigation of external fan cowl separation for compact nacelles in windmilling scenarios

Sabnis, Kshitij

AIAA

Sabnis K, Boscagli L, Babinsky H, et al., (2023) Experimental investigation of external fan cowl separation for compact nacelles in windmilling scenarios. In: 2023 AIAA Aviation and Aeronautics Forum and Exposition (AIAA AVIATION Forum), 12-16 June 2023, San Diego, CA
https://doi.org/10.2514/6.2023-3394